MIT Libraries | DSpace@MIT

MIT Open Access Articles

CO2 reduction and methane partial oxidation on surface catalyzed La0.9Ca0.1FeO3-# oxygen transport membranes

Massachusetts Institute of Technology

CO$_2$ reduction and methane partial oxidation on surface catalyzed La$_{0.9}$Ca$_{0.1}$FeO$_{3-\delta}$ oxygen transport membranes

Xiao-Yu Wu[*], Ahmed F. Ghoniem

Department of Mechanical Engineering, Massachusetts Institute of Technology, 77 Massachusetts Avenue, Cambridge, MA 02139, USA

[*] Address: 3-339N, 77 Massachusetts Avenue, Cambridge, MA, 02139, USA

Email: xywu@mit.edu (X.Y. Wu)

Submit to **OTHER CONCEPTS** Colloquium

Total length of the paper: 5660 by Method 1

Word Equivalent length for each item

Items	Length	Items	Length
Main text	3124.0	Equation 1	22.8
Reference	454.5	Equation 2	22.8
Figure 1	191.0	Equation 3	22.8
Figure 2	242.4	Equation 4	22.8
Figure 3	163.2	Equation 5	22.8
Figure 4	158.2	Equation 6	45.6
Figure 5	185.4	Equation 7	22.8
Figure 6	284.9	Equation 8	30.4
Figure 7	286.2	Equation 9	30.4
Table 1	197.6	Equation 10	22.8
Table 2	60.8	Equation 11	22.8
		Equation 12	22.8

Abstract

In this paper, we demonstrate CO_2 thermochemical reduction to CO in a $La_{0.9}Ca_{0.1}FeO_{3-\delta}$ oxygen ion transport membrane reactor. For process intensification, we also show that methane can be used on the sweep side, producing two streams: a CO stream from CO_2 reduction on the feed side, and a syngas stream on the other. We show that surface reactions are the rate-limiting steps for fuel-assisted CO_2 reduction on a flat LCF-91 membrane. To improve productivity, we study how that adding catalytic porous layers can accelerate these steps and hence, increase the CO_2-to-fuel conversion rates. Adding LCF-91 porous layers onto the membrane surface raised the oxygen flux increased by 1.4X. Secondly, different catalysts ($Ce_{0.5}Zr_{0.5}O_2$ on the feed side and $(La_{0.6}Sr_{0.4})_{0.95}Co_{0.2}Fe_{0.8}O_3$ on the sweep side) were added onto the porous layers to further accelerate the surface reaction rates. As a result, the oxygen flux was further increased especially at lower temperatures, e.g., at 850°C, oxygen flux was raised by one order of magnitude as compared to the unmodified membrane. Process intensification was tested on the latter membrane configuration, and the syngas produced on the sweep side had a H_2:CO ratio very close to 2, ideal for production of fuels. Carbon species balance showed that higher methane concentration on the sweep side could lead to coke formation. Results also show that the selectivity to CO_2 near the membrane surface is higher than that at the reactor outlet due to the availability of lattice oxygen and the favorable water-gas shift reactions.

2

1. Introduction

CO$_2$ capture, utilization and storage (CCUS) have both environmental and economic benefits [1, 2]. CO$_2$ can be injected into depleted gas and oil wells to enhance resource recovery, and it can be converted to fuels and chemicals using renewable energy to close the carbon loop while using fossil fuel [3]. Different methods have been proposed for CO$_2$-to-fuel, e.g., thermochemical redox cycles [4, 5] and oxygen ion transport membrane-assisted CO$_2$ reduction [6, 7]. Compared with the redox cycle, the membrane reactor has several advantages: it has fewer moving parts at elevated temperatures and can shift the thermodynamic equilibrium for CO$_2$ reduction. Process intensification can also be achieved on this membrane by integrating CO$_2$ reduction and partial oxidation of methane (POM) on the feed and sweep sides, respectively, as shown in Fig 1. Because the overall process is endothermic and elevated temperatures are required, renewable heat sources, such as concentrated solar thermal energy can be utilized. Hence, this process can be considered as an energy storage technology that converts renewable thermal energy into chemical energy for storage in pipes or tanks. Furthermore, the overall result of this process intensification is methane dry reforming. However, instead of producing syngas with H$_2$:CO = 1 as a single stream in a packed bed reactor from methane dry reforming, two streams of more valuable gases are produced in the membrane reactor: one is CO on the feed side, the other is syngas with H$_2$:CO = 2 on the sweep side. The first can be used as a fuel, while the second stream provides syngas composition that is optimal for the production of methanol and higher hydrocarbons [8]. Using a membrane also avoids the need for extra components such as an air separation unit upstream or gas separation equipment downstream of the reformer. Thus, the co-production plant can be more compact and efficient.

Several oxygen ion transport membranes have been proposed, mainly for air separation or oxy-fuel combustion, e.g., perovskites (with ABO$_3$ chemical formula) such as BaCo$_x$Fe$_y$Zr$_{1-x-y}$O$_{3-\delta}$ (BCFZ) and La$_{0.6}$Sr$_{0.4}$Co$_{0.2}$Fe$_{0.8}$O$_{3-\delta}$ (LSCF) [9, 10]. Most of the high performance materials contain Ba or Sr in the A site [10]. Ba or Sr-containing perovskites are not stable in CO$_2$ environment as they suffer from degradation due to the formation of stable carbonates, which decrease the active surface area and

reduce the oxygen flux [11]. On the other hand, Ca-containing membranes are less prone to forming carbonates. Based on the Ellingham diagram, $CaCO_3$ decomposes spontaneously at 1 atm CO_2 at temperatures above 850°C [11]. Yet these membranes were reported to have lower oxygen flux [10, 12, 13]. Efforts are needed to identify the rate-limiting steps during CO_2 reduction and examine novel approaches to improve the permeation process in the stable membranes.

In this work, we investigate the integration of CO_2 reduction and methane partial oxidation on surface modified $La_{0.9}Ca_{0.1}FeO_{3-\delta}$ (LCF-91) membranes. LCF-91 has been shown to be stable in CO_2 and reducing environments [12-14], and our previous studies show that surface reactions on both sides can be rate-limiting when fuel is added on the sweep side [7]. Here, our first goal is to demonstrate that the CO_2 reduction rates can be enhanced by facilitating these rate-limiting surface reactions such as adding porous structures and catalysts. Secondly, we demonstrate the integrated process intensification on the modified LCF-91 membrane. The CO_2 reduction rates on the feed side, syngas H_2:CO ratio and coke formation on the sweep side are reported and discussed.
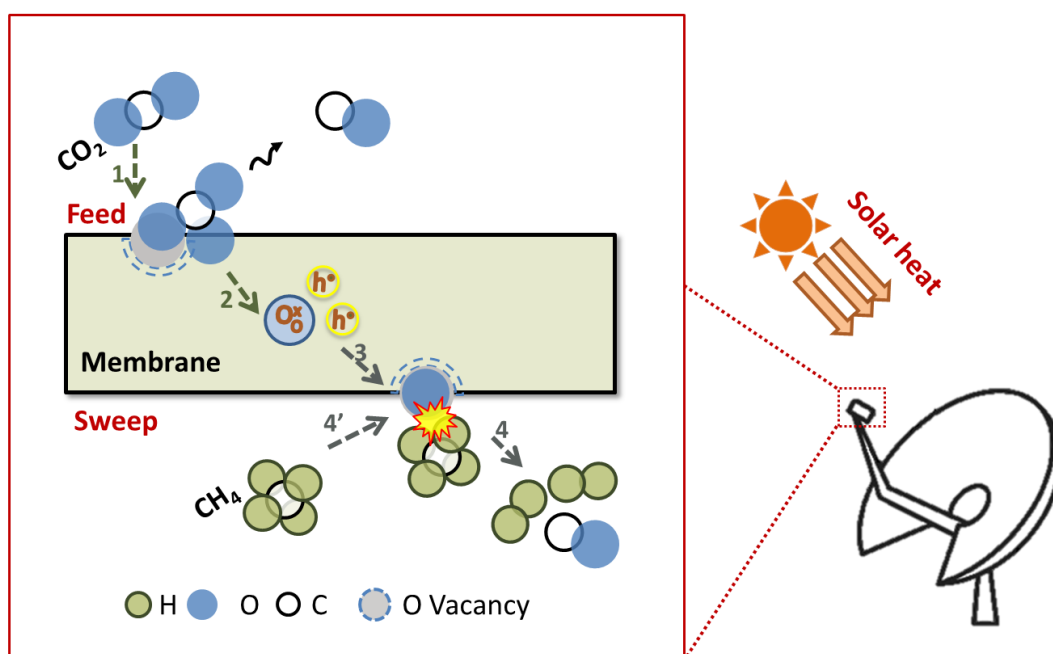

4

Figure 1 Schematic of integrated process intensification (i.e., CO_2 reduction and partial oxidation of methane) in an oxygen permeable membrane reactor. Concentrated solar energy is used as an example for renewable heat source

2. Experiments

2.1 Experimental setup

A button-cell membrane reactor with axis-symmetric reverse flow is used. A schematic diagram of the reactor is shown in Fig. 2. An oxygen permeable membrane is sandwiched between two alumina tubes. 24k gold sealant from Lux Bond & Green is used to seal the membrane to the alumina tubes, which can endure elevated temperatures and reactive environments. The membrane reactor is located inside a furnace, and the temperature is monitored with K-type thermocouples and controlled with a proportional–integral–derivative (PID) controller. A quartz capillary probe (from Restek) with 0.53 mm OD is inserted into the center of the sweep side of the membrane reactor, with the tip touching the membrane surface. Using a probe was sufficient for the purpose of determining the gas species concentrations very close to the surface, as shown in our previous papers [12-14]. Gas samples from the probe and the inlets/outlets of the reactor are examined using two gas chromatographers (GC), i.e., 490 Micro GC and Shimadzu GC2014 with the thermal conductivity detector (TCD). The error bars in the data reported later represent the range of measured values due to experimental uncertainties. The gas flow rates on both sides of the membrane reactor are controlled by mass flow controllers (MFC) from Brooks Instrument ®. Different carrier gases on the feed and sweep sides are used to monitor the leak across the membrane during experiments. Besides, no CO leakage around the membrane was observed during experiments. More detailed construction and use of the reactor can be found in our previous papers [13, 15].
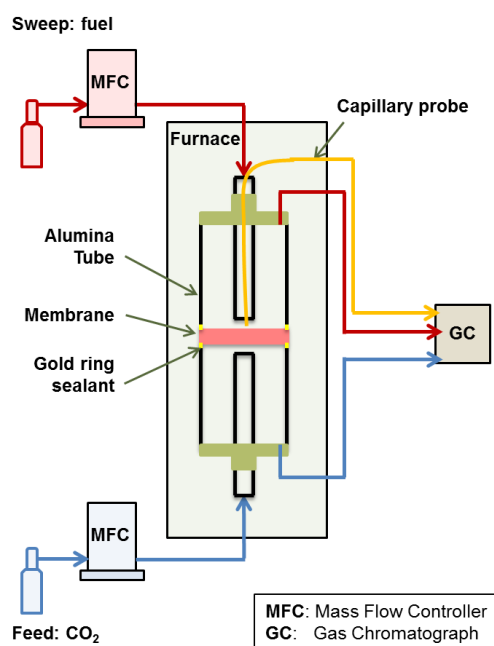
Figure 2 The schematic shows the test apparatus. A capillary probe is inserted on the sweep side of the reactor to sample the gas species very close to the membrane surface

2.2 Membrane configurations

The unmodified dense LCF-91 perovskite membranes (Membrane 1 in Table 1) were fabricated by Ceramatec. The effective diameter of the membrane is 12.7 mm, the same as the inner diameter of the alumina tubes. To investigate the acceleration of the surface reactions, two designs, i.e., Membranes 2 and 3 were systematically performed by modifying the chemical compositions of the porous layers. First, catalytic porous layers were added on both sides in our lab using a two-step method (Membrane 2 in Table 1). LCF-91 powders (particle specific surface area 1.8 m^2/g, density 6.4 g/cm^3, from Ceramatec) were mixed with graphite powders at 50 vol% (particle size <20 μm, from Sigma-Aldrich®) in mortar and pestle for twenty minutes. The mixed powders (0.24 g) were then compressed into a flat circular pellet at 10 metric ton-force for one minute. Following that, the as-pressed pellet was attached to the flat dense membrane and together they were sintered at 1450°C for half an hour in air (including slow heat-up and cool down at ramp rates around 10°C, the entire process took around 24 hours).

Table 1

Summary of membrane configurations

	Membrane #	1	2	3
Dense	Thickness [mm]	1.3	1.3	1.3
	Effective diameter [mm]	12.7	12.7	12.7
Porous layer – feed side	Thickness [mm]	/	0.3	0.78 ± 0.11
	Diameter [mm]	/	12.69 ± 0.4	12.43 ± 0.38
	Composition	/	LCF-91	LCF-91 + 20% mol CZO
Porous layer – sweep side	Thickness [mm]	/	0.3	0.43 ± 0.02
	Diameter [mm]	/	12.42 ± 0.8	11.86 ± 0.28
	Composition	/	LCF-91	LCF-91 + 20% mol LSCF

In another membrane configuration (Membrane 3 in Table 1), catalysts were added onto the porous layers using the same two-step method with a powder mixture of catalysts, LCF-91 and graphite. The mass, diameter and volume of the graphite particles of the as-pressed pellets are the same as those on Membrane 2. $Ce_{0.5}Zr_{0.5}O_2$ (CZO) has been shown to catalyze CO_2 splitting in the range of 600 – 900°C [4] and hence, it was added onto the feed side (99.0% purity, from Sigma-Aldrich®). Besides, $(La_{0.6}Sr_{0.4})_{0.95}Co_{0.2}Fe_{0.8}O_3$ (LSCF), known for its good redox kinetics and high vacancies concentration [16], was added on the sweep side to enhance methane partial oxidation (particle specific surface area is 10-14 m^2/g, from Fuel Cell Materials). The dimensions and compositions of all the membranes are summarized in Table 1.

2.3 Data deduction

The CO concentration at the outlet of the feed chamber, $X'_{CO,out}$, [-], is measured by the gas chromatographer, and the CO production rate from CO_2 thermochemical reduction is calculated as

$$Y_{CO} = X'_{CO,out} \times n' \qquad (1)$$

where Y_{CO} is the yield of CO, [mol s^{-1}], and n' is total molar flow rate, [mol s^{-1}].

As the CO_2 thermochemical reduction rate is low, we assume that all the oxygen produced diffuses through the membrane. Hence, the oxygen flux is related to the CO yield, as

$$J_{O_2} = Y_{CO} / (2A_{memb}) \qquad (2)$$

where J_{O2} is the oxygen flux, [mol cm^{-2} s^{-1}], and A_{memb} is effective membrane surface area, [cm^2]. The CO_2 thermochemical reduction rate (or CO_2-to-fuel rate, $J_{CO2\text{-to-fuel}}$, [mol cm^{-2} s^{-1}]) is twice of the oxygen flux.
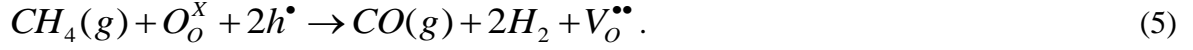
3 Results and discussion

3.1 Flux enhancement by the catalytic porous layers

For fuel-assisted CO_2 thermochemical reduction on LCF-91 membranes, previous studies showed that surface reactions on both sides are the rate-limiting steps, with CO_2 reduction on the feed side being the slowest step at low temperatures, while it being the fuel oxidation on the sweep side at high temperatures [7]. The reactive surface areas should be increased to accelerate the surface reactions. Porous layers made of the same LCF-91 perovskite were added onto both sides using the two-step method described in section 2.2 (Membrane 2 in Table 1) to expand the active membrane surface. On the feed side, the active sites are the oxygen vacancies on the membrane surface based on the CO_2 direct incorporation mechanism [17],

$$CO_2(g) + V_O^{\bullet\bullet} \rightarrow CO(g) + O_O^X + 2h^\bullet. \qquad (3)$$

Here, Kröger–Vink notation is used. $V_O^{\bullet\bullet}$ is the lattice oxygen vacancy, O_O^X is the lattice oxygen, $h^\bullet$ is the electron hole, or more precisely the net charge in the lattice iron atoms. On the other hand, lattice

oxygen is an active site for fuel oxidation on the sweep side according to the Mars-van Krevelen (MvK) mechanism with CO (model fuel) or methane [18],

$$CO(g) + O_O^X + 2h^\bullet \rightarrow CO_2(g) + V_O^{\bullet\bullet},$$ (4)

$$CH_4(g) + O_O^X + 2h^\bullet \rightarrow CO(g) + 2H_2 + V_O^{\bullet\bullet}.$$ (5)

We use a single step overall reaction to illustrate the active sites, while multi-step mechanisms have been proposed in the literature for CO and methane oxidation on oxides [19]. The oxygen fluxes for Membrane 2 with CO sweep are shown in Fig. 3. Compared with the unmodified Membrane 1, an increase of oxygen flux by ~0.02 μmol cm^{-2} s^{-1} can be observed.
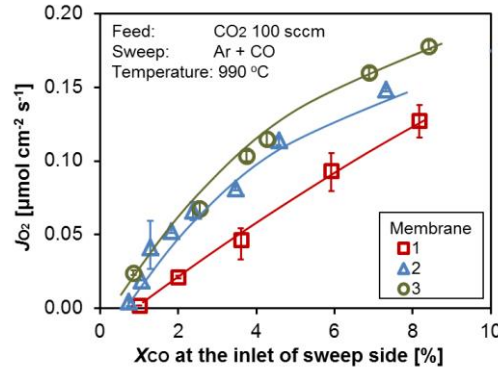

Figure 3 The oxygen fluxes associated with CO_2 reduction for the three membrane configurations tested at various fuel concentrations on the sweep side

The oxygen flux through Membrane 2 can be described using the resistance-network model developed in [15, 20] and the reaction rate constants obtained in our previous work [7]. Here, the effectiveness factors η_f and η_s of the porous layers on the feed and sweep sides, respectively, are used to evaluate the surface reaction rates. Hence, the flux is,

$$J_{O_2} = \frac{1}{2} \cdot \frac{C_O}{\dfrac{1}{\eta_f \dfrac{A_f}{A_c} k_{f,CO_2} C'_{CO_2}} + \dfrac{t}{D_V} + \dfrac{1}{\eta_s \dfrac{A_s}{A_c} k_{r,CO_2} C''_{CO}}}.$$ (6)

Here C_o is the total site concentration for oxygen species (accounting for both oxygen atoms and vacancies) on LCF-91 materials, which is assumed to have a constant value: 0.0825 mol cm^{-3}, estimated from XRD measurements of stoichiometric LCF-91 lattice in air [21]. t is the thickness of the dense membrane, [cm] and D_v is the oxygen diffusivity, [cm^2 s^{-1}]. A_c is the surface area of the flat membrane, [cm^2]. k_{f,CO_2}, [cm^4 mol^{-1} s^{-1}] and k_{r,CO_2}, [cm^4 mol^{-1} s^{-1}], are the reaction rate constants for reactions (3) and (4), respectively. C'_i and C''_i are the concentrations of gas species i on the feed and sweep side surfaces, respectively, [mol cm^{-3}].

The effectiveness factor, η, is defined as the ratio of the overall reaction rate in the porous layer to the reaction rate on the layer's outmost surface. It can be approximated based on the generalized function of the Thiele Modulus, ϕ, for simple reactions[22], as

$$\eta = \left(\tanh \phi \right)/\phi . \tag{7}$$

The Thiele Modulus is the ratio of the reaction rate over the diffusion rate in the porous layer,

$$\phi^2 = \frac{r_{surf}}{D_{AB,e}\left(C_{A0}/L_c\right)} = \frac{J_{O_2} L_c}{D_{AB,e} C_{A0}} . \tag{8}$$

Here r_{surf} is the overall reaction rate on the porous surface, [mol cm^{-2} s^{-1}], $D_{AB,e}$ is the effective diffusivity between gas species A and B, [cm^2 s^{-1}], and C_{A0} is the concentration of gas species A on membrane surface, [mol cm^{-3}], L_c is characteristic length of the porous layer, [cm], i.e., the layer thickness, and J_{O2} is the oxygen flux, [mol cm^{-2} s^{-1}]. In the membrane reactor setup, the overall reaction rate on the surface equals to the oxygen flux through the membrane under steady state conditions.

As there is high concentration of CO_2 (~100%) and Ar (>90%) on the feed and sweep sides, respectively, binary diffusion coefficients are used to model the gas diffusion on each side. The effective diffusivity of the gas species in the porous layer is,

$$D_{AB,e} = \frac{\varphi_p \sigma_c}{\tilde{\tau}} D_{AB} = \varepsilon_D D_{AB} , \tag{9}$$

where φ_p is the porosity of the layer, [-], σ_c is the constriction factor, [-], $\tilde{\tau}$ is the tortuosity, [-], D_{AB} is the binary diffusion coefficients between species A and B[23], [cm^2 s^{-1}], and ε_D is the coefficient to

10

be fitted using the experimental data. Both surface layers are made from the same mixtures (LCF-91 + 50 vol% graphite) by the same procedure, so the pore structures should be the same, which is shown in the scanning electron microscope (SEM) images in Fig. S1. Large pores with diameter in the order of 10 μm are randomly distributed in the porous layer. Grains with sizes of ~1 μm formed large clusters in the order of ~50 μm after sintering. The porosity of the layers are estimated to be 0.25 (see supporting information).

Based on the experimental data, the total surface areas A_f and A_s on the feed and sweep sides, respectively, [cm^2] and the coefficient ε_D are fitted by minimizing the absolute sum of the relative error between the measured oxygen flux and that evaluated using Eq. (6). The values are shown in Table 2. Although the total surface areas, A_f and A_s are assumed to be different in the expression used to fit the data, the fitted values are very close as both porous layers were fabricated with the same procedure. The oxygen fluxes are within ±25% accuracy between the experimental and fitted values (the goodness of the fitting is shown in Fig. S2 in the Supporting Information).

Table 2

Fitted properties of the porous layers

Property	Unit	Value
A_f	[cm^2]	2.12
A_s	[cm^2]	2.19
ε_D	[-]	6.29×10^{-3}

Based on the fitted values, the Thiele modulus for the porous layers on the feed and sweep sides are calculated to be in the orders of magnitude of $0.1 - 1$, while those on the sweep side are higher and closer to 1, as shown in Fig. 4. This shows that the mass diffusion and the reaction rates in the pores are of the similar orders of magnitude and hence, both are important in determining the effectiveness of the porous layer on accelerating the surface reaction rates. Further investigation of the

gas diffusion into the porous layer coupled with the surface reactions is needed to optimize the porous layer structures for the membrane reactor.
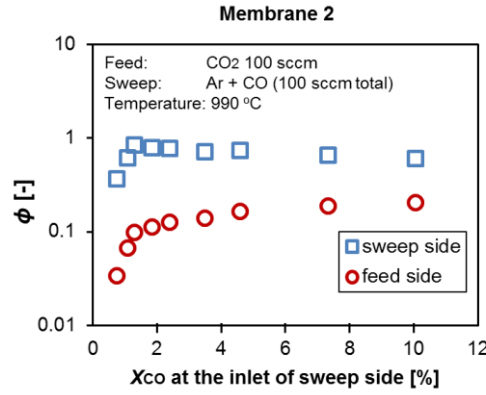

Figure 4 The Thiele Modulus for the porous layers on the feed and sweep sides on Membrane 2

To further accelerate the surface reactions, porous layers of 20mol% CZO + 80mol% LCF and 20mol% LSCF + 80mol% LCF were added on the feed and sweep sides, respectively, on Membrane 3. CZO catalyzes CO_2 reduction thanks to its fast oxygen mobility and low defect formation energy [4], while LSCF has good redox kinetics and high vacancies concentration to facilitate fuel oxidation [16]. As a result, the oxygen fluxes are further increased compared to Membrane 2, with the maximum oxygen flux reaching 0.18 μmol cm^{-2} s^{-1} at 990°C. The porous layers of Membrane 3 are thicker than those of Membrane 2 (shown in Table 1). Because mass diffusion and surface reaction rates are on similar orders of magnitude, the thicker porous layers of Membrane 3 may be one reason for the small enhancement by adding 20mol% catalysts. Another reason could be the additional resistance from the oxygen diffusion and the electron conduction between the catalysts and the LCF-91 support:

$$CO_2(g) + V_{O,CZO}^{\bullet\bullet} + 2e_{CZO}^{'} \rightarrow CO(g) + O_{O,CZO}^{X} \tag{10}$$

$$O_{O,CZO}^{X} + V_{O,LCF}^{\bullet\bullet} \rightarrow V_{O,CZO}^{\bullet\bullet} + 2e_{CZO}^{'} + O_{O,LCF}^{X} + 2h_{LCF}^{\bullet} \tag{11}$$

Here, $V_{O,j}^{\bullet\bullet}$ and $O_{O,j}^{X}$ are the oxygen vacancy and the lattice oxygen oxide j. e'_{CZO} and $h_{LCF}^{\bullet}$ are the electron/hole species.
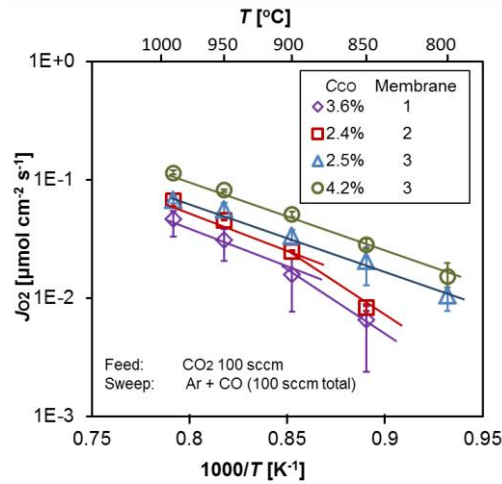
12

Figure 5 Arrhenius plot of the oxygen fluxes on different membrane configurations under various fuel inlet concentration (C_{CO}) on the sweep side, [dimensionless]

CO$_2$ reduction rates at various fuel inlet concentrations were tested. The dependence of the oxygen flux on temperatures showed the same trend for each membrane configuration, as can be seen in Fig. S3. Here, we compare the two cases (i.e., C_{CO} = 2.5% and ~4%) in Fig. 5. For the unmodified Membrane 1, the plot shows a slope change at around 900°C, due to the transition of the limiting step from CO$_2$ splitting on the feed side to CO oxidation on the sweep side [7]. Similarly, Membrane 2 also shows the transition of the slope at the same temperature. Yet for Membrane 3, the slope is constant across 800 – 1000 °C (and as expected, independent of CO concentration) showing improvements in CO$_2$ reduction. Membrane 3 has fluxes higher than Membrane 1; especially at lower temperatures like 850°C, the increase reaches about one order of magnitude (C_{CO} = ~4% case), thanks to the CZO and LSCF catalysts on Membrane 3 [4, 16, 24]. Further enhancement can be achieved by redesigning the porous layer to decrease mass transfer barrier and using a better catalyst on the membrane surface and membrane materials with higher oxygen fluxes.

3.2 Process intensification with methane partial oxidation

13

Processes intensification with CO_2 reduction and POM is demonstrated using Membrane 3. Methane sweep increases the oxygen flux by creating larger chemical potential gradient across the membrane [12], while utilizing the permeated oxygen to produce syngas. As shown in Fig. 6a, the oxygen fluxes rises with the methane inlet concentrations to 0.25 µmol cm^{-2} s^{-1}. Comparing the CH_4 and CO sweep cases, the fluxes are very close at low fuel inlet concentrations. At higher concentrations, the oxygen fluxes with CH_4 sweep are higher, as methane full oxidation is more likely to occur near the membrane surface [13], creating more oxygen vacancy and higher driving force for the oxygen diffusion.

The maximum CO_2 reduction ratio in this work is 0.92% when methane inlet concentration is 10.3%. This value is low, due to the small membrane dimension tested (1.27 cm^2). Assuming the flux is proportional to the membrane surface, an area of 131 cm^2 is required to achieve 95% CO_2 reduction.
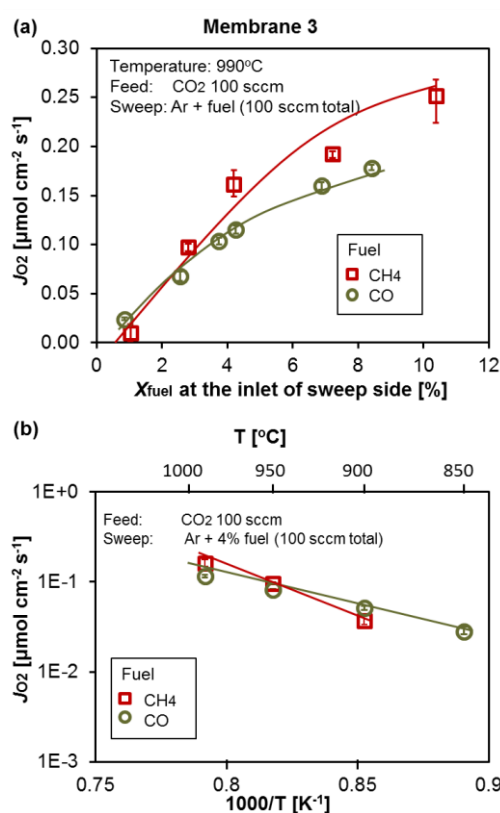
Figure 6 (a) The oxygen fluxes associated with the intensified process, comparing with CO sweep cases, and (b) Arrhenius plot of the oxygen fluxes over temperatures are shown

Figure 6b shows that compared to the CO sweep case, methane sweep has slightly higher apparent activation energy, which can be due to the high activation energy for methane oxidation on LCF-91 [7, 13]. This also confirms that at high operating temperature, the rate-limiting step is the fuel oxidation on the sweep side, similar to Membrane 1[20].

The products of methane partial oxidation on the sweep side are shown in Fig. 7. The outlet syngas concentration shows a H_2:CO ratio around 2, optimal for gas-to-liquid process. With high methane concentration at the inlet, the H_2:CO ratio is slightly higher than 2. Figure 7b shows that the selectivity to CO_2, S''_{CO_2} is very close to zero at the outlet of the reactor,

$$S''_{CO_2} = n''_{CO_2} \Big/ \left(n''_{CO_2} + n''_{CO_2} \right),$$
(12)

where n''_i is the molar flow rate of the species i on the sweep side, [mol s^{-1}]. Thus, CO is the major carbon oxidation product at the reactor outlet. The deviation of H_2:CO ratio from stoichiometry can be due to CH_4 pyrolysis producing coke and hydrogen. The pyrolysis at high methane inlet concentration is confirmed by the gas phase carbon balance plot in Fig. 7a, which is defined as the ratio between the gas phase carbon flow rates at the outlet and the inlet. The unbalanced gas phase carbon at higher methane concentration indicates coke formation.

Figure 7b shows the selectivity to CO_2 is as high as 40% near the membrane surface, while the value drops to less than 3.5% at the outlet. The concentrations of the gas species were measured using the capillary probe with the tip touching the membrane surface, which is illustrated earlier in Section 2.1. This confirms that near the membrane surface, full oxidation of carbon species is more likely due to the high concentration of lattice oxygen and the reverse water-gas shift reaction. As CO_2 diffuses away from the membrane surface and flows to the outlet, it reacts with methane in the gas phase by dry reforming. Hence, S''_{CO_2} drops at the outlet.
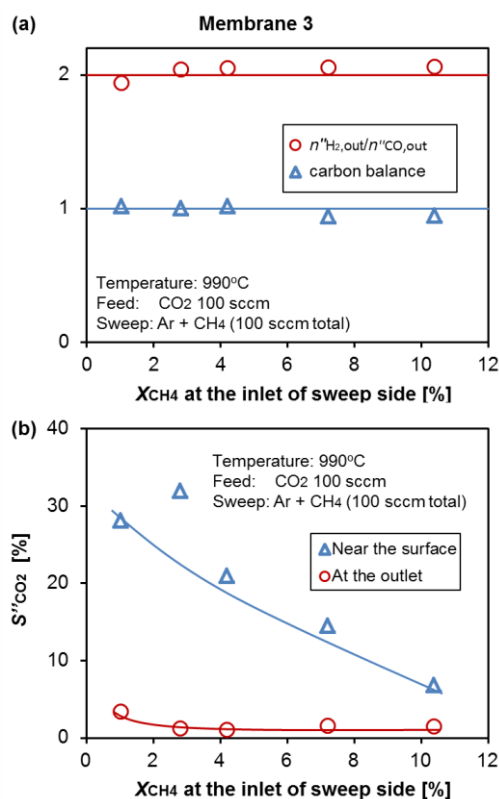
Figure 7 (a) The CO:H_2 ratio and the gas phase carbon balance, and (b) The selectivity to CO_2 near the surface and at the outlet of the sweep side are shown

4. Conclusions

In this paper, we demonstrate the process integration of CO_2 reduction and methane partial oxidation on a LCF-91 oxygen permeable membrane reactor. Two membrane designs (i.e., Membranes 2 and 3) were systematically performed by modifying the chemical compositions of the catalytic porous layers. The porous layers increase the CO_2 reduction rate by accelerating the surface reactions, which are shown to be the rate-limiting steps. We observe the following:

(1) The LCF-91 porous layers on the feed and sweep sides (Membrane 2) raise the oxygen flux by about 0.02 μmol cm^{-2} s^{-1} compared with the unmodified Membrane 1. Arrhenius plots of the oxygen flux show a change in the slope, or apparent activation energy with temperatures. This indicates that at higher temperatures there is a transition between the limiting steps from CO_2 splitting on the feed side to CO oxidation on the sweep side, similar to Membrane 1. The Thiele Modulus for the porous

layers on the feed and sweep sides are $0.1 - 1$, and hence, the gas diffusion and reaction rates in the porous layers are in similar orders of magnitude.

(2) Catalysts are added to the porous layer ($Ce_{0.5}Zr_{0.5}O_2$ on the feed side and $(La_{0.6}Sr_{0.4})_{0.95}Co_{0.2}Fe_{0.8}O_3$ on the sweep side of Membrane 3) to further increase the oxygen fluxes by around 0.01 µmol $cm^{-2}s^{-1}$ at 990^oC. The increase of slope at low temperatures is not observed for this membrane from the Arrhenius plot. At lower temperatures like 850^oC, the oxygen flux is increased by an order of magnitude thanks to the catalysts in the porous layer on Membrane 3 compared with the unmodified Membrane 1 under similar fuel concentrations on the sweep side.

(3) Process intensification of CO_2 reduction to fuel and methane partial oxidation is demonstrated on Membrane 3. The maximum oxygen flux measured is 0.25 µmol $cm^{-2}s^{-1}$ with 10.4% methane at the sweep side inlet. The syngas produced on the sweep side has a $H_2:CO$ ratio very close to the optimal value of 2 for methanol and higher hydrocarbon production. This results from a combination of the heterogeneous reactions on the membrane surface and the homogeneous reactions in the bulk. The gas carbon species balance shows that at higher methane inlet concentration, coking occurs due to pyrolysis, which slightly increases the $H_2:CO$ ratio of the syngas produced on the sweep side. Results also show that the selectively to CO_2 near the membrane surface is higher than that at the reactor outlet.

Acknowledgment

References

[1] A.F. Ghoniem, Prog. Energy Combust. Sci. 37 (1) (2011) 15-51.
[2] M. Beller, G. Centi, L. Sun, ChemSusChem 10 (1) (2017) 6-13.
[3] A.W. Kleij, M. North, A. Urakawa, ChemSusChem 10 (6) (2017) 1036-1038.
[4] Z. Zhao, M. Uddi, N. Tsvetkov, B. Yildiz, A.F. Ghoniem, PCCP 19 (37) (2017) 25774-25785.
[5] F. Lin, M. Rothensteiner, I. Alxneit, J.A. van Bokhoven, A. Wokaun, Energy Environ. Sci. 9 (7) (2016) 2400-2409.

[6] M. Tou, R. Michalsky, A. Steinfeld, Joule 1 (1) (2017) 146-154.

[7] X.Y. Wu, A.F. Ghoniem, ChemSusChem 11 (2) (2018) 483-493.

[8] NETL, available at <http://www.netl.doe.gov/research/coal/energy-systems/gasification/gasifipedia/syngas-optimization>

[9] R. Falkenstein-Smith, P. Zeng, J. Ahn, Proceedings of the Combustion Institute 36 (3) (2017) 3969-3976.

[10] J. Sunarso, S. Baumann, J.M. Serra, W.A. Meulenberg, S. Liu, Y.S. Lin, J.C. Diniz da Costa, J. Membr. Sci. 320 (1-2) (2008) 13-41.

[11] K. Efimov, T. Klande, N. Juditzki, A. Feldhoff, J. Membr. Sci. 389 (0) (2012) 205-215.

[12] G. Dimitrakopoulos, A.F. Ghoniem, Proceedings of the Combustion Institute *in press* (2016).

[13] X.-Y. Wu, A.F. Ghoniem, M. Uddi, AlChE J. 62 (12) (2016) 4427-4435.

[14] G. Dimitrakopoulos, A.F. Ghoniem, J. Membr. Sci. 529 (2017) 114-132.

[15] X.Y. Wu, L. Chang, M. Uddi, P. Kirchen, A.F. Ghoniem, PCCP 17 (15) (2015) 10093-10107.

[16] H.J. Hwang, J.-W. Moon, S. Lee, E.A. Lee, J. Power Sources 145 (2) (2005) 243-248.

[17] C. Argirusis, F. Voigts, P. Datta, J. Grosse-Brauckmann, W. Maus-Friedrichs, PCCP 11 (17) (2009) 3152-3157.

[18] E.W. McFarland, H. Metiu, Chem. Rev. 113 (6) (2013) 4391-4427.

[19] E.S. Hecht, G.K. Gupta, H. Zhu, A.M. Dean, R.J. Kee, L. Maier, O. Deutschmann, Applied Catalysis A: General 295 (1) (2005) 40-51.

[20] S.J. Xu, W.J. Thomson, Chem. Eng. Sci. 54 (17) (1999) 3839-3850.

[21] G. Pecchi, M.G. Jiliberto, A. Buljan, E.J. Delgado, Solid State Ionics 187 (1) (2011) 27-32.

[22] G.F. Froment, J.D. Wilde, K.B. Bischoff, Chemical Reactor Analysis and Design, 3rd ed, Wiley, Hoboken, N.J. , 2011 p. 193 - 197

[23] E.N. Fuller, P.D. Schettler, J.C. Giddings, Industrial & Engineering Chemistry 58 (5) (1966) 18-27.

[24] Z. Zhao, M. Uddi, N. Tsvetkov, B. Yildiz, A.F. Ghoniem, The Journal of Physical Chemistry C 121 (21) (2017) 11055-11068.

List of figures

List of tables